Correction of phase distortion in spatial heterodyne spectroscopy

Christoph R. Englert, John M. Harlander, Joel G. Cardon, and Fred L. Roesler

The detailed analysis of measured interferograms generally requires phase correction. Phase-shift correction methods are commonly used and well documented for conventional Fourier-transform spectroscopy. However, measured interferograms can show additional phase errors, depending on the optical path difference and signal frequency, which we call phase distortion. In spatial heterodyne spectroscopy they can be caused, for instance, by optical defects or image distortions, making them a characteristic of the individual spectrometer. They can generally be corrected without significant loss of the signal-to-noise ratio. We present a technique to measure phase distortion by using a measured example interferogram. We also describe a technique to correct for phase distortion and test its performance by using a simulation with a near-UV solar spectrum. We find that for our measured example interferogram the phase distortion is small and nearly frequency independent. Furthermore, we show that the presented phase-correction technique is especially effective for apodized interferograms. © 2004 Optical Society of America

OCIS codes: 300.6300, 120.6200, 120.2650.

1. Introduction

Spatial heterodyne spectroscopy (SHS) is a relatively novel concept that, when compared with other spectroscopic techniques such as Fabry–Perot or Michelson interferometers, can offer many advantages for high-spectral-resolution diffuse-source spectroscopy. It was conceived in the late 1980's and was made possible primarily by the availability of detector arrays, e.g., the charge-coupled device (CCD), in combination with high computing speed to process the recorded interferogram data.[1]

The basic SHS configuration is similar to a Michelson interferometer with the return mirrors replaced by fixed diffraction gratings. It contains no moving parts and can be field widened with fixed prisms in the interferometer arms to increase the étendue of the instrument by as much as 2 orders of magnitude over conventional Fabry–Perot or scanning Michelson interferometers. Detailed descriptions of SHS can be found in publications by Harlander *et al.*[1–3]

Figure 1 shows the basic, non-field-widened SHS configuration. A major difference between conventional Fourier-transform spectrometers and SHS is that in SHS all interferogram points are recorded simultaneously by an array of detectors, whereas a Fourier-transform spectrometer records the interferogram samples with a single detector in a time series during which the scan mirror is moving. In a Fourier-transform spectrometer, light from the entire aperture of the interferometer is focused on a single detector element. This drives the need for flat, homogenous interferometer optics and a well-controlled scanning mechanism because variations in optical path difference across the interferometer aperture of more than a fraction of a wavelength greatly reduce the detected fringe contrast and the signal-to-noise ratio of the spectrum. In the SHS configuration, the fringe localization plane near the gratings is focused onto the imaging detector, as illustrated for one detector element in Fig. 1. Consequently, the signal for each interferogram element uses only a small area of the gratings, beam splitter, and the exit optics before it reaches the detector. Variations in optical flatness across the aperture result primarily in a phase distortion in the interferogram and produce fringes that are not straight and equally spaced; however, the fringes

C. R. Englert and J. G. Cardon are with the U.S. Naval Research Laboratory, Space Science Division Code 7641, 4555 Overlook Avenue, S.W., Washington, D.C. 20375. J. M. Harlander is with the Department of Physics, Astronomy and Engineering Science, St. Cloud State University, 720 Fourth Avenue South MS-315, St. Cloud, Minnesota 56301. F. L. Roesler is with the Department of Physics, 1150 University Avenue, University of Wisconsin–Madison, Madison, Wisconsin 57306.
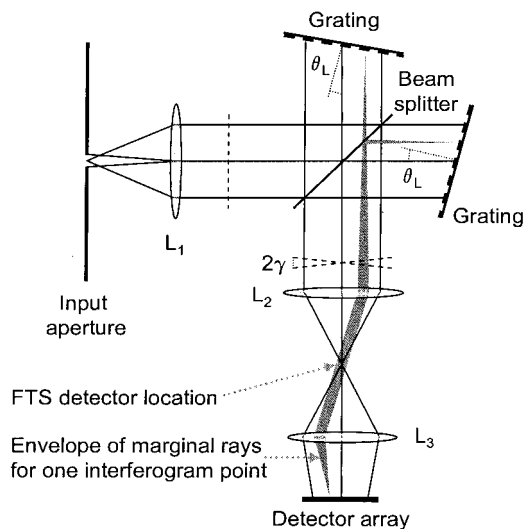
Fig. 1. Schematic diagram of the basic non-field-widened SHS configuration. The dashed lines illustrate an incoming wave front and the corresponding exiting wave fronts, which are crossed with an angle of 2γ. The ray bundle for one interferogram element is outlined, showing that only a small section of the interferometer and optics are used for any individual interferogram element. FTS, Fourier-transform spectrometer.

are recorded with high contrast as long as the interferometer elements are good over the small area sampled by each detector pixel. These phase distortions are analogous to nonuniform path difference sampling in Fourier-transform spectroscopy (FTS). Another potential cause for phase distortion in a SHS interferogram is the image distortion of the exit optics, which reimages the fringe localization plane on the detector array. These phase distortions have no obvious equivalent in FTS. Generally, significant phase distortion can and should be avoided in any SHS instrument design. If, however, an instrument shows significant phase distortion,[4] it is a characteristic of the spectrometer and can generally be corrected without significant loss of the signal-to-noise ratio in the measured data during the postprocessing of the interferogram. The SHS concept therefore poses relaxed flatness, index homogeneity, and alignment requirements compared with a Fourier-transform spectrometer. Moreover, optical defects, for example, a scratch on the grating, have only a localized effect on the interferogram, which allows for their isolation and proper treatment in the processing of the interferogram.

In the following section we revisit the basics of the SHS interferogram as a basis for the subsequent discussion on how to determine the phase distortion for a given spectrometer. As an example, an interferogram measured with the Spatial Heterodyne Imager for Mesospheric Radicals–Space Shuttle Middeck (SHIMMER–MIDDECK) instrument[3] is used. Finally, correction techniques for different types of phase distortion are discussed by use of model calculations of a near-UV solar spectrum.

2. Spatial Heterodyne Spectroscopy Interferogram

Figure 1 illustrates the basic process by which a SHS interferogram is created. Incoming wave fronts are split into the two interferometer arms, and the returning diffracted wave fronts recombine at the beam splitter. The recombining wave fronts are parallel and coincident for only one wave number, the Littrow wave number (σ_0), which produces a constant signal across the detector. For wave numbers different from the Littrow wave number, the exiting wave fronts are crossed as shown in Fig. 1, resulting in a fringe pattern that is recorded by the detector array. For wave numbers close to the Littrow wave number, the spatial frequency of the fringes is directly proportional to the wave-number difference ($\delta\sigma = \sigma_0 - \sigma$), so that the modulated portion of the detected signal is the Fourier transform of the incident spectral distribution heterodyned around the Littrow wave number.[1]

For the following discussion of phase distortion, we introduce the fundamental form of a SHS interferogram, in which x is the location of an individual detector element in the dispersion plane [$x = 0$ is the point of stationary phase, i.e., the location of zero path difference (ZPD)], κ is proportional to the heterodyned wave number, $\delta\sigma$, and $\Phi(\kappa, x)$ is an additive phase-distortion term:

$$I(x) = \int_{-\infty}^{\infty} A(\kappa, x)\beta(\kappa)(\exp\{i[\kappa x + \Phi(\kappa, x)]\}$$
$$+ \exp\{-i[\kappa x + \Phi(\kappa, x)]\})\mathrm{d}\kappa. \qquad (1)$$

The goal is to retrieve the spectral intensity $\beta(\kappa)$ from the interferogram, which is the sum of cosine fringes with the amplitude $\beta(\kappa)$ multiplied by a normalized envelope function $A(\kappa, x)$. If the envelope function is unity and the phase-distortion term, $\Phi(\kappa, x)$, is zero, a simple Fourier transform yields $\beta(\kappa)$ for $\kappa > 0$ and $\beta(-\kappa)$ for $\kappa < 0$. The effect of the envelope function is that the retrieved spectrum is convoluted with the Fourier transform of the envelope function. This effect is familiar from FTS and contributes to the finite resolution of measured spectra and the instrumental line-shape function in general. In SHS the envelope function depends on wave-number-independent contributions such as the finite detector size and wave-number-dependent contributions such as the modulation transfer function of the imaging optics. In the following we do not investigate the effects of $A(\kappa, x)$ further because they are similar to FTS. Instead, we focus on the effect of the phase term.

3. Measuring Phase Distortion

A. Method

The overall approach to determine phase distortion is to use measurements of a monochromatic source.

Table 1. Key Design Parameters of the SHIMMER–MIDDECK Instrument

Attribute	Design Value
Spectral filter	2.3 nm FWHM centered at 308.9 nm
Resolving power	53,500
Spectral resolution	58×10^{-3} Å
Maximum étendue (without optics transmission)	96×10^{-3} cm^2 sr

For a monochromatic source, the modulated portion of the interferogram I_{κ_0} can be written as

$$I_{\kappa_0}(x) = A(\kappa_0, x)\beta(\kappa_0)(\exp\{i[\kappa_0 x + \Phi(\kappa_0, x)]\}$$
$$+ \exp\{-i[\kappa_0 x + \Phi(\kappa_0, x)]\}). \quad (2)$$

If the phase-distortion term varies slowly with x, the Fourier transform of I_{κ_0}, $\mathbf{F}(I_{\kappa_0})$, has nonzero values only in the vicinity of κ_0 and $-\kappa_0$, corresponding to the two exponential functions in Eq. (2). By multiplying $\mathbf{F}(I_{\kappa_0})$ with a window function that removes the signal at and around $-\kappa_0$, we can isolate the signal around κ_0, and, after backward transformation, we get

$$I_{\kappa_0}(x) = A(\kappa_0, x)\beta(\kappa_0)\exp\{i[\kappa_0 x + \Phi(\kappa_0, x)]\}. \quad (3)$$

The total phase for κ_0 can then be obtained by

$$\kappa_0 x + \Phi(\kappa_0, x) = \arctan\{\Im[I_{\kappa_0}(x)]/\Re[I_{\kappa_0}(x)]\}, \quad (4)$$

where $\Im$ and $\Re$ extract the imaginary and real parts of their respective arguments. By subtracting the first term from the left side of Eq. (4), one can determine the phase distortion for the wave number of the monochromatic source. To determine the phase distortion as a function of wave number, $\Phi(\kappa, x)$, one can repeat the procedure with monochromatic sources of different wave numbers. Most convenient is a tunable monochromatic source. As an alternative, one can use a source with well-separated unresolved lines. Isolating the different lines in $\mathbf{F}(I)$, as described above, then yields the same result as with a true monochromatic source.

At this point, we also mention that the shape of the envelope function $A(\kappa_0, x)$ can be obtained from Eq. (3) in that $\beta(\kappa_0)$ is a scalar and the exponent of the exponential function is known from the first term in Eq. (4). The investigation of the wave-number-dependent envelope function is useful to understand the wave-number-dependent instrumental line-shape function of a given interferometer.

B. Example

As an example for a measurement of the phase distortion of a SHS spectrometer, we use the SHIMMER–MIDDECK instrument that flew on the Space Shuttle Atlantis (STS-112) in October 2002[3,5] and a manganese–neon (MnNe) hollow-cathode lamp as the source. The SHIMMER–MIDDECK instrument measures double-sided interferograms with a UV-sensitive CCD. Some key design specifications of this instrument are listed in Table 1. Figure 2 shows the power spectrum (relative intensity versus

fringe frequency) of the MnNe lamp within the passband of the spectrometer around 309 nm. We determined the spectrum by transforming the modulated part of the measured interferogram after correcting it for detector offset (bias and dark) and a flat field. From the 32 interferograms that SHIMMER–MIDDECK images simultaneously on the CCD,[3] interferogram number 16 was chosen for this example. This interferogram was recorded along a CCD row near the center of the two-dimensional array. The power spectrum in Fig. 2 also includes the negative spatial frequencies, which result directly from the Fourier transform of the interferogram. The spectral filter blocks any real signal at negative frequencies (see Table 1). The spectral resolution of the measurement is approximately 58 mÅ.

The MnNe spectrum features several atomic lines. Four of these lines, identified as A, B, C, and D in Fig. 2, were chosen for the determination of the wave-number-dependent phase distortion. They were selected because they are strong and interference of neighboring lines is minimal. Details about the selected lines are given in Table 2.

Following the method described above, we now isolate the individual lines. We chose to multiply the complex spectrum with normalized Gaussian functions centered on the maximum intensity of the lines and a full width at half-maximum (FWHM) of 9.7 spectral elements. The isolation functions are shown in gray and referenced to the right ordinate in Fig. 2. Backward transformation of the isolated lines yields $I_{\kappa_0}(x)$ for each line, and we can now cal-
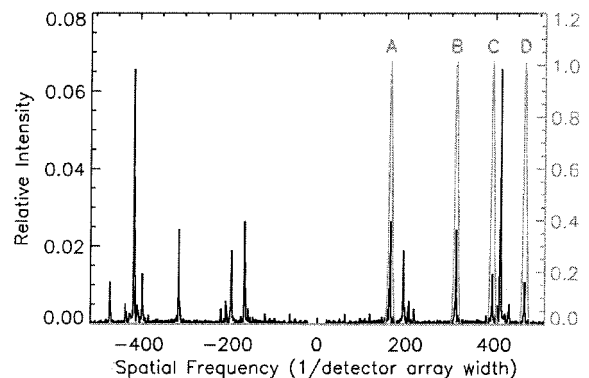

Fig. 2. Black curve, power spectrum of a MnNe hollow-cathode lamp as measured by the SHIMMER–MIDDECK instrument versus spatial frequency of the recorded fringes. Gray curve, Gaussian functions (FWHM = 9.7 spectral elements) used to isolate individual emission lines in order to determine the frequency-dependent phase distortion.

Table 2.   Emission Lines Selected for This Study

Identifier	Emitter	Line position[6] (nm)
A	Mn I	307.9642
B	Ne II	308.8170
C	Ne II	309.2901
D	Ne II	309.7133

culate the total phase $[\Phi(\kappa_0, x) + \kappa_0 x]$ for each line by using Eq. (4).

We define phase shift as the phase at $x = 0$ (near the ZPD). This phase shift can be considered to be the value of the phase-distortion function at $x = 0$. The phase shift for our example spectrum is shown in Fig. 3 as a function of the wavelength. The near-linear wavelength dependence is familiar from FTS and is the result of effects such as the dispersion within the interferometer or the sampling grid, which generally does not include the ZPD location. For increased clarity of the following considerations, we subtract the phase shift from the total phase of the emission-line interferograms so that all measured phase functions are zero at $x = 0$.

To determine the phase distortion, $\Phi(\kappa_0, x)$, from Eq. (4), we need to determine $\kappa(\sigma)$, where σ is the wave number of the signal. This is equivalent to the frequency calibration of the spectrometer. In our example, we fit a phase plane $\Omega[\kappa(\sigma), x]$ to the phase functions of the four emission lines. $\Omega[\kappa(\sigma), x]$ assumes a linear relationship between the heterodyned wave number and κ:

$$\Omega(\sigma, x) = \kappa(\sigma)x = C(\sigma - \sigma_0)x. \quad (5)$$

The two fit parameters are σ_0, the Littrow wave number, and C, a constant. The result of the fit is shown in Fig. 4. In this three-dimensional plot the measured, phase-shift-corrected phase functions of the four emission lines are plotted as bold solid lines with the fitted phase plane overplotted in gray. For the Littrow wave number σ_0, the phase function is zero for each pixel. For pixel number 0, near the ZPD, the phase function is zero for all wave numbers because we phase shift corrected the measured phase functions. The fit results in a Littrow wave number σ_0 of 32570.4 cm^{-1} ($\lambda = 307.027$ nm) and a C of

Fig. 4.   Bold, solid traces are the phase-shift-corrected total phase functions of the four MnNe emission lines listed in Table 2. The gray mesh is the phase plane that is fitted to the four phase functions. The two fit parameters are the Littrow wave number σ_0, where the phase function is zero, and the parameter C, which is the linear slope increase of the phase functions with respect to the heterodyned wave number ($\sigma_0 - \sigma$); see also Eq. (4).

0.0101412 [(rad/cm^{-1})/pixel width], which corresponds to a grid spacing of approximately 58 mÅ in the spectrum and a maximum bandwidth of approximately 2.97 nm for 1024 interferogram samples.

At this point we can determine the phase distortion $\Phi(\kappa_0, x)$, which, according to Eq. (4), is the residual of the measured phase functions and the phase plane plus the phase shift that we subtracted before the fit.

Figure 5 shows the phase-shift-corrected phase distortion for the four emission lines in the MnNe spectrum. The data show that there is little phase distortion around the ZPD location ($x = 0$), but a small additional phase component is apparent for all four wave numbers toward higher optical path difference. The data do not show a strong wave-number dependence of the phase distortion, as indicated by the similarity of the four curves. The slight wave-
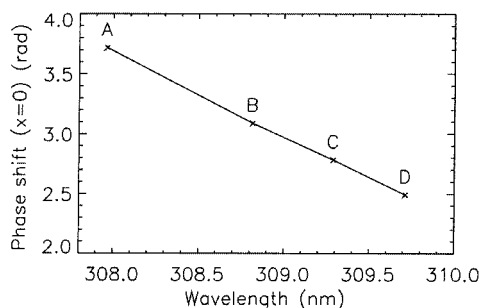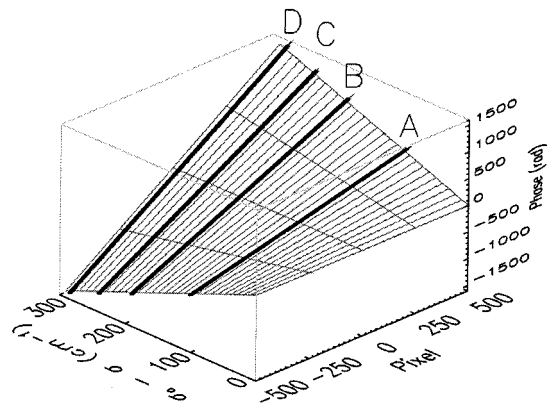

Fig. 3.   Phase shift near the ZPD point for the four MnNe emission lines. The naming of the lines (A, B, C, D) follows from Fig. 2 and Table 2.
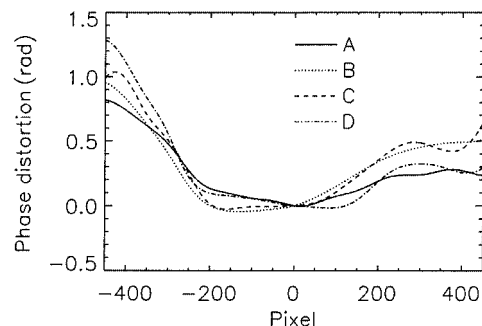

Fig. 5.   Phase-shift-corrected phase distortion for the four emission lines listed in Table 2. All graphs are zero for pixel 0 owing to the phase-shift correction. The phase distortion does not show a significant frequency dependence (the curves basically fall on top of one another). The smoothness of the curves is caused by the narrow Gaussian isolation functions shown in Fig. 2. The phase distortion is small in the center of the detector array, and the maximum phase distortion is less than a fringe (2π), even for line D, which has the highest spatial frequency (~467 fringes per detector width) of the four lines.

number dependence is possibly caused by the interference of neighboring lines.

The smoothness of the phase distortion in Fig. 5 is a direct consequence of the narrow Gaussian isolation function. Ideally, a monochromatic source is used to determine the phase distortion, so that a narrow isolation function is not necessary to suppress neighboring lines; thus the phase distortion can be determined with higher resolution. However, as long as the phase distortion is sufficiently slowly varying, a high-resolution measurement of its variation should not be necessary.

If significant phase distortion is present for a given SHS instrument, it is characteristic of the spectrometer and can generally be corrected for in the postprocessing of the interferogram with little impact on the signal-to-noise ratio. In the following, we discuss several types of phase error and possible correction techniques.

4. Phase Shift [$\Phi = \phi_\kappa(\kappa)$]

The case in which the phase term in Eq. (1) is a function of wave number only [$\Phi = \phi_\kappa(\kappa)$] is commonly known as phase shift. Possible causes for phase shift are an uncompensated beam splitter or a sampling grid that does not include the exact zero path location of the measured interferogram. Phase shift has been discussed widely in the FTS literature, so we mention only some key aspects of it and refer the reader to the references for details.

Equation (1) shows that a phase shift is equivalent to a multiplication of the recovered spectrum by $\exp[i\phi_\kappa(\kappa)]$ for $\kappa > 0$ and $\exp[-i\phi_\kappa(\kappa)]$ for $\kappa < 0$. The simplest correction method is to calculate the absolute value of the retrieved spectrum, also called the power spectrum. This operation ensures that the entire spectral information is again contained in the real part of the recovered spectrum; however, it has a nonlinear effect on the measurement noise[7] because both the real and the imaginary noise components contribute to the power spectrum.

Better correction techniques are based on a determination of $\phi_\kappa(\kappa)$ from the double-sided part of the interferogram by use of the fact that the spectrum by definition has no imaginary part. Generally, the multiplication of the spectrum[8] with $\exp[i\phi_\kappa(\kappa)]$ or the equivalent convolution in the interferogram domain[7] will yield the phase-corrected spectrum. Especially for one-sided interferograms and emission-line spectra, the phase-shift correction has to be performed carefully to avoid the introduction of intensity and absolute line position errors. Further details about phase-shift correction can be found in the FTS literature.[7–10]

5. Frequency-Independent Phase Distortion [$\Phi = \phi_x(x)$]

The case in which the phase term in Eq. (1) is a function of optical path difference only [$\Phi = \phi_x(x)$] is not typical for FTS but can be found in narrowbandpass SHS systems. It can be caused, for example, by grating figure errors or index inhomogeneities in the interferometer. The phase error $\phi_x(x)$ can be

determined from a single interferogram of one monochromatic source as described by Harlander *et al.*[2] or from a multiline source as discussed previously in this paper. Correcting a frequency-independent phase distortion[2] can be achieved by a multiplication of the interferogram in Eq. (1) with $\exp[-i\phi_x(x)]$, which yields

$$I'(x) = \int_{-\infty}^{\infty} A(\kappa, x)\beta(\kappa)\exp[i(\kappa x)] + A(\kappa, x)\beta(\kappa)$$

$$\times \exp\{-i[\kappa x + 2\phi_x(x)]\}d\kappa. \qquad (6)$$

The first term is identical to the corresponding term in the interferogram without any phase error. Its Fourier transform is the spectrum $\beta(\kappa)$ for $\kappa > 0$. Here the instrumental line-shape function is the Fourier transform of the envelope function $A(\kappa, x)$, which remains unchanged. The second term in Eq. (6) acquires twice the phase error, and the Fourier transform of this term results in $\beta(\kappa)$ for $\kappa < 0$ convoluted with the Fourier transform of $A(\kappa, x)\exp[-2i\phi_x(x)]$. If this corrupted envelope function is a slowly varying function of x, its Fourier transform will be localized, i.e., confined to low-frequency components. In this case the second term in Eq. (6) will have only a small effect on the $\kappa > 0$ part of the Fourier transform of $I'(x)$, which then contains the complete, corrected spectral information. The $\kappa < 0$ part can be ignored.

According to the convolution theorem of Fourier transformation, the multiplication with $\exp[-i\phi_x(x)]$ in Eq. (6) is equivalent to the convolution with the Fourier transform of $\exp[-i\phi_x(x)]$ in the spectral domain. For slowly varying phase distortions the convolution kernel $F\{\exp[-i\phi_x(x)]\}$ has the advantage of being localized in the spectral domain (see below).

6. Frequency-Dependent Phase Distortion [$\Phi = \phi(x, \kappa)$]

The case of the frequency-dependent phase distortion is the most general case. The previously discussed cases are included in this case.

A possible cause for frequency-dependent phase distortion is image distortion by the exit optics (L_2 and L_3 in Fig. 1). If image distortion is present, the fringe pattern at the detector still appears in focus, but the magnification of the image changes across the detector array. As a consequence, the fringe frequency from a monochromatic source changes across the detector array. In this case, the resulting phase distortion is proportional to the fringe frequency. In our previously discussed example, image distortion would cause the phase distortion of line D (~467 fringes per detector width) to be approximately 2.8 times the phase distortion of line A (~164 fringes per detector width). Figure 5 does not show this behavior, which indicates that, for this instrument, image distortion is not the dominant contribution to the phase distortion.

The correction of the frequency-dependent phase distortion has to be performed in the spectral domain because the correction is different for each wave number and the interferogram samples carry information

of all wave numbers at the same time. In the case of the frequency-independent phase distortion we found, at the end of Section 5, that the correction can be performed in the spectral domain via a convolution with a correction function. Here we will apply a similar technique.

To correct for the frequency-dependent phase distortion, we first calculate the Fourier transform of $\exp[-i\phi(x, \kappa)]$ for each κ, which we call $G_\kappa(\kappa')$:

$$G_\kappa(\kappa') = F(\exp\{-i[\phi(x, \kappa)]\}). \quad (7)$$

Then we correct the spectrum $\beta_U(\kappa')$ that results from the Fourier transformation of the uncorrected interferogram by convolving it with $G_\kappa(\kappa')$:

$$\beta_C(\kappa) = \int_{-\infty}^{\infty} \beta_U(\kappa'')G_\kappa(\kappa - \kappa'')d\kappa''. \quad (8)$$

In the strict mathematical sense, this is only a convolution if the function $G_\kappa(\kappa')$ is independent of κ, which is the case of frequency-independent phase distortion, and it is equivalent to the correction technique previously discussed for that case. Here the convolution function depends on κ. However, if the phase distortion is slowly varying with x and κ, $G_\kappa(\kappa')$ will also vary slowly with κ, and all $G_\kappa(\kappa')$ functions are nonzero only around $\kappa' = 0$. This means that locally (around each κ in the spectrum) the conditions are similar to a real convolution, and good correction results can be achieved with this technique. In Section 7 we will illustrate this technique by using the highly structured, near-UV solar spectrum as an example.

7. Simulated Performance of Frequency-Dependent Phase-Distortion Correction with a Near-UV Solar Spectrum

To assess the performance of the frequency-dependent phase-distortion correction discussed above, we take a high-resolution near-UV solar spectrum,[11] multiply it with a filter transmittance centered at approximately 309 nm, and bin it into 513 frequency bins with a width of 60 mÅ. These parameters have been chosen because they are similar to the parameters of the SHIMMER instruments.[3,12] By use of Eq. (2) as a model, synthetic interferograms were generated for this spectrum for the various phase-distortion functions described below. Figure 6, panel A (6A), shows the spectrum without any phase distortion.

The first simulation uses a set of phase-distortion functions that are a superposition of a frequency-independent contribution and a function that is proportional to the frequency and to the fourth power of the pixel number to simulate image distortion. Figure 6B shows three phase-distortion functions for the frequencies marked σ_I, σ_{II}, and σ_{III} in Fig. 6A. The leftmost, black marking in Fig. 6A corresponds to the Littrow frequency. Figure 6C shows the real part of the uncorrected spectrum that is retrieved by the Fourier transform of the phase-distorted interfero-
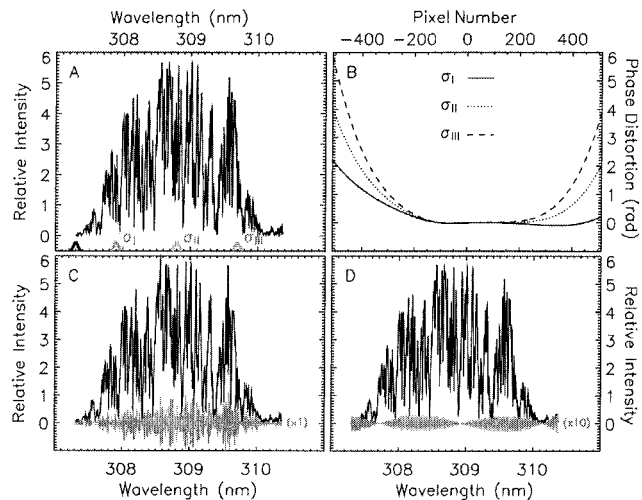

Fig. 6. First simulation case: high spectral resolution and nonperiodic phase distortion. A: high-resolution solar spectrum multiplied with a typical interference filter transmittance. The leftmost, black mark indicates the Littrow frequency, and gray marks indicate the frequencies for which the phase-distortion functions are plotted in panel B. B: phase-distortion functions for the frequencies marked in panel A. C: black curve, real part of the uncorrected, phase-distorted spectrum. Gray, residuals between the uncorrected spectrum and the initial spectrum. D: black curve, phase-distortion-corrected spectrum. Gray, residuals between the phase-distortion-corrected spectrum and the initial spectrum multiplied by 10.

gram. It also shows the residuals with respect to the initial spectrum (Fig. 6A) in gray. Figure 6D shows the phase-corrected spectrum and the residuals multiplied by 10 in gray. The correction has improved the residuals by more than an order of magnitude, but a systematic residual at the 1% level is still apparent. The correction is not complete because it relies on the assumption that the convolution functions (the Fourier transform of the phase-distortion functions) are slowly varying with frequency and quickly falling off to zero away from the center. The phase-distortion functions and corresponding convolution functions that we used for the first simulation violate mainly the second assumption. The convolution functions in this simulation do not show rapid convergence to zero away from the center because the phase distortion for the lowest frequency is significantly different from that at the highest frequency and the discrete Fourier transform of this discontinuity results in significant ringing.

One can avoid this behavior by choosing phase-distortion functions that have the same value for the highest and lowest frequencies, as seen in Fig. 7B. As a result, the residuals (Fig. 7D) of the corrected spectrum improve significantly. Of course, this is not a real option for a given spectrometer, in which the phase-distortion functions cannot be changed easily. Another, more practical way to improve the performance of the correction is to reduce the resolution of the spectrum, for example by apodizing the interferogram. The lower-resolution spectrum will
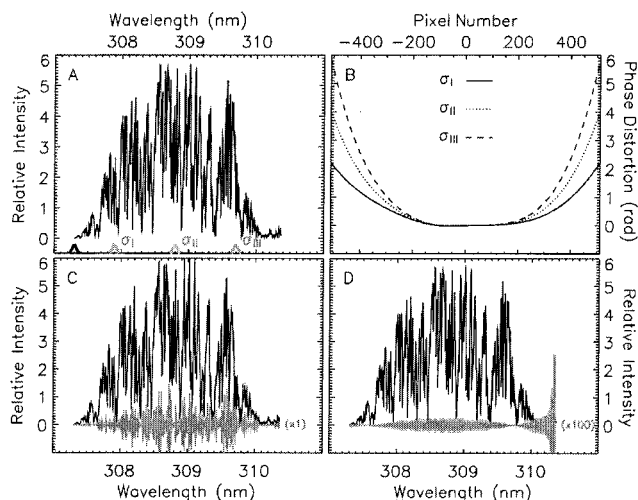
Fig. 7. Second simulation case: high spectral resolution and periodic phase distortion. A: high-resolution solar spectrum multiplied with a typical interference filter transmittance. The leftmost, black mark indicates the Littrow frequency, and the gray marks indicate the frequencies for which the phase-distortion functions are plotted in panel B. B: phase-distortion functions for the frequencies marked in panel A. C: black curve, real part of the uncorrected, phase-distorted spectrum. Gray, residuals between the uncorrected spectrum and the initial spectrum. D: black curve, phase-distortion-corrected spectrum. Gray, residuals between the phase-distortion-corrected spectrum and the initial spectrum multiplied by 100. The residuals are more than an order of magnitude smaller than in the first simulation case (Fig. 6).
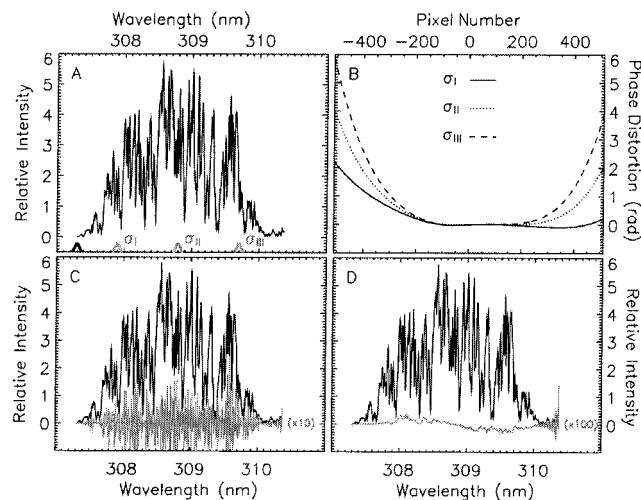

Fig. 8. Third simulation case: lower spectral resolution and nonperiodic phase distortion. A: high-resolution solar spectrum convolved with the kernel $(\frac{1}{4}, \frac{1}{2}, \frac{1}{4})$, which is equivalent to an interferogram apodization with a Hanning function, multiplied with a typical interference filter transmittance. The leftmost, black mark indicates the Littrow frequency, and the gray marks indicate the frequencies for which the phase-distortion functions are plotted in panel B. B: phase-distortion functions for the frequencies marked in panel A. C: black curve, real part of the uncorrected, phase-distorted spectrum. Gray, residuals between the uncorrected spectrum and the initial spectrum multiplied by 10. D: black curve, phase-distortion-corrected spectrum. Gray, residuals between the phase-distortion-corrected spectrum and the initial spectrum multiplied by 100. The residuals are more than an order of magnitude smaller than in the first simulation case (Fig. 6) and well below the 1% level.

effectively minimize the contributions of the high-frequency ringing of the convolution function in Eq. (8). However, the price of lower spectral resolution has to be paid. Figure 8A shows the solar spectrum convoluted with the line-shape function that corresponds to an interferogram apodization with a Hanning function. For this case, the residuals of the corrected spectrum are well below the 1% level (see Fig. 8D).

Many spectra are calculated with apodized interferograms from the start to achieve a well-localized instrumental line-shape function rather than a sinc line-shape function that also includes significant ringing. In case the loss in resolution by apodizing the interferogram is not acceptable, the phase-distortion term can be included in a frequency-dependent instrumental line-shape function for further data analysis.

8. Conclusion

Interferograms measured by SHS instruments may show phase distortion depending on the instrument design and implementation. If significant phase distortion is present for a given instrument, it can generally be corrected without significant loss of the signal-to-noise ratio. We presented a method to determine the frequency-dependent phase distortion and applied it to a measurement of a UV SHS instrument by using a multiline source. For this case, we found the phase distortion to be small (less than a fringe even for the highest spatial frequencies) and virtually frequency independent. We subsequently simulated three phase-correction cases by using the UV solar spectrum around 309 nm with different spectral resolutions and different phase-distortion functions. We verified that the correction method works well if the phase distortion varies slowly with frequency and if the Fourier transform of the phase-distortion functions falls off quickly for higher frequencies. Since the second assumption is not necessarily true, e.g., if the phase-distortion functions are not periodic, we showed that decreasing the resolution of the spectrum (apodizing the interferogram) improves the quality of the correction.

Small phase distortions like the ones in our example should be the goal of every SHS spectrometer design but are not always easy to achieve.[4] In these cases the proper correction gains in importance.

References
1. J. M. Harlander, R. J. Reynolds, and F. L. Roesler, "Spatial heterodyne spectroscopy for the exploration of diffuse inter-

stellar emission lines at far ultraviolet wavelengths," Astrophys. J. **396,** 730–740 (1992).

2. J. M. Harlander, H. T. Tran, F. L. Roesler, K. P. Jaehnig, S. M. Seo, W. T. Sanders, and R. J. Reynolds, "Field-widened spatial heterodyne spectroscopy: correcting for optical defects and new vacuum ultraviolet performance tests," in *EUV, X-Ray, and Gamma-Ray Instrumentation for Astronomy V*, O. E. Siegmund and J. Vallerga, eds., Proc. SPIE **2280,** 310–319 (1994).

3. J. M. Harlander, F. L. Roesler, J. G. Cardon, C. R. Englert, and R. R. Conway, "SHIMMER: a spatial heterodyne spectrometer for remote sensing of Earth's middle atmosphere," Appl. Opt. **41,** 1343–1352 (2002).

4. B. E. Laubscher, B. W. Smith, B. J. Cooke, P. C. LaDelfe, R. R. Berggren, P. V. Villeneuve, R. M. Goeller, G. M. Obbink, S. Milligan, J. W. Howard, P. R. Norton, M. Stegall, C. B. Burgett, J. M. Harlander, and R. F. Horton, "Infrared imaging spatial heterodyne spectrometer (IRISHS) experiment effort," in *Infrared Imaging Systems: Design, Analysis, Modeling, and Testing, X*, G. C. Holst, ed., Proc. SPIE **3701,** 194–205 (1999).

5. J. G. Cardon, C. R. Englert, J. M. Harlander, F. L. Roesler, and M. H. Stevens, "SHIMMER on STS-112: development and proof-of-concept flight," in *AIAA Space 2003 Conference and Exposition* (American Institute of Aeronautics and Astronautics, Reston, Va., 2003), AIAA paper 2003-6224.

6. W. C. Martin, J. R. Fuhr, D. E. Kelleher, A. Musgrove, L. Podobedova, J. Reader, E. B. Saloman, C. J. Sansonetti, W. L. Wiese, P. J. Mohr, and K. Olsen, "NIST Atomic Spectra Database (version 2.0, 1999)," http://physics.nist.gov/asd.

7. M. L. Forman, W. H. Steel, and G. V. Vanesse, "Correction of asymmetric interferograms obtained in Fourier spectroscopy," J. Opt. Soc. Am. **56,** 59–63 (1966).

8. J. W. Brault, "High precision Fourier transform spectroscopy: the critical role of phase correction," Mikrochim. Acta **3,** 215–227 (1987).

9. R. C. M. Learner, A. P. Thorne, I. Wynne-Jones, J. W. Brault, and M. C. Abrams, "Phase correction of emission line Fourier transform spectra," J. Opt. Soc. Am. A **12,** 2165–2171 (1995).

10. D. B. Chase, "Phase correction in FT-IR," Appl. Spectrosc. **36,** 240–244 (1982).

11. R. L. Kurucz, I. Furenlid, J. Brault, and L. Testerman, *National Solar Observatory Atlas No. 1*, (Harvard University, Cambridge, Mass., 1984).

12. J. M. Harlander, F. L. Roesler, C. R. Englert, J. G. Cardon, R. R. Conway, C. M. Brown, and J. Wimperis, "Robust monolithic ultraviolet interferometer for the SHIMMER instrument on STPSat-1," Appl. Opt. **42,** 2829–2834 (2003).